Spontaneous symmetry lowering of Si (001) towards two-dimensional ferro/antiferroelectric behavior

Chengcheng Xiao,[1] Xinwei Wang,[1] Xiaodong Pi,[1] Shengyuan A. Yang,[2] Yuanping Feng,[3] Yunhao Lu,[1,4,*] and Shengbai Zhang[5]

[1]*State Key Laboratory of Silicon Materials, School of Materials Science and Engineering, Zhejiang University, Hangzhou 310027, China*
[2]*Research Laboratory for Quantum Materials, Singapore University of Technology and Design, Singapore 487372, Singapore*
[3]*Department of Physics, National University of Singapore, Singapore 117542, Singapore*
[4]*Department of Physics, Zhejiang University, Hangzhou 310027, China*
[5]*Department of Physics, Applied Physics, and Astronomy, Rensselaer Polytechnic Institute, Troy, New York 12180, USA*

(Received 20 November 2018; revised manuscript received 11 March 2019; published 24 April 2019)

Electronic polarization, manifested in numerous physical phenomena such as ferroelectricity, piezoelectricity, and pyroelectricity, is of great importance to many technological applications. The presence of ferroelectricity in bulk elemental materials is extremely rare due to the high symmetry of the underlying lattices. However, the presence of a surface lowers the symmetry, which may provide a future avenue for achieving robust ferroelectric polarization. Using first-principles calculations, we show that a spontaneous electrical polarization can be realized on the silicon reconstructed (001) surface. The magnitude of this polarization is 0.45×10^{-10} C/m, comparable to those in benchmarking two-dimensional ferroelectric compounds such as SnTe and SnSe. The symmetry lowering is originated from a Peierls instability that removes the degeneracy of surface dangling bonds, whereby opening a band gap. Although flip-flop of the surface dimers may destroy the ordered phase at elevated temperatures, we find that a modest compressive strain, which increases the local stress and interdimer coupling, can drastically increase the robustness of the ferroelectric state towards room-temperature operations. The technology for processing Si has been well developed and the Si (001) surface has also been widely used in various electronic devices. Our discovery here thus holds high promise in a multitude of fields, ranging from nanoscale random access memory to low power consumption energy storage devices.

DOI: 10.1103/PhysRevMaterials.3.044410

Ferroelectric materials have attracted significant interest due to their wide applications in the semiconductor industry such as nonvolatile memories, sensors, and nanoscale electronic devices [1,2]. Recently, ultrathin two-dimensional (2D) ferroelectric group-IV monochalcogenides like SnSe and SnTe have been predicted and experimentally shown to exhibit ferroelectricity (FE) even above room temperature [3–6]. Robust ferroelectricity has also been predicted by our group for group-V elemental semiconductors [7] driven by a reduction in resonant bonding [8,9], and for few-layer tellurium due to interlayer interactions mediated by lone pairs [10].

For a nonmetal to have robust FE, two conditions must be met: (1) the system must be noncentrosymmetric and have spontaneous electronic polarization, and (2) there must exist two or more equivalent atomic configurations which can be effectively switched by an external electric field. The most challenging issue in finding FE in elemental systems (i.e., materials with a single element) is that most known phases for nonmetallic elemental systems are centrosymmetric, which prohibits a finite spontaneous polarization. In contrast, symmetry is generally lowered at material surfaces, where the lattice periodicity is abruptly interrupted. Naturally, one may wonder: *Is it possible to achieve FE on a particular surface of an elemental material?*

In this paper, we provide a concrete answer to the above question. We report spontaneous electrical polarization for the reconstructed Si (001) surface, which is one of the most studied surfaces for its importance in the semiconductor industry. Curiously, however, to the best of our knowledge, the issue of ferro/antiferroelectricity for this system has never been addressed before. Previous studies have shown that the stable configuration of the Si (001) surface has two equivalent asymmetric dimer structures [11], which in fact hints at the possible emergence of a spontaneous polarization. Indeed, using *ab initio* method, we show that the distortion associated with the dimer structure generates a spontaneous in-plane electric polarization, with a magnitude of 10^{-10} C/m. To study the temperature effects, we link the polarization to local structures by a 2D Ising model and carry out Monte Carlo (MC) simulations. Our results agree well with previous theoretical and experimental studies in terms of the transition temperature (T_c) and the flip-flop motion of surface dimers [12,13]. The model further predicts hysteresis loops as functions of temperature and strain, which can be tested by experiment. By revealing a surprising ordering parameter, i.e., the hidden ferro/antiferroelectricity, of a well-known surface system in a well-developed technology, the findings here could have significant impacts on developing functional electronic devices.

The low-temperature structures of the silicon (001) surface have been extensively studied in the past. Both experiment

*Corresponding author: luyh@zju.edu.cn

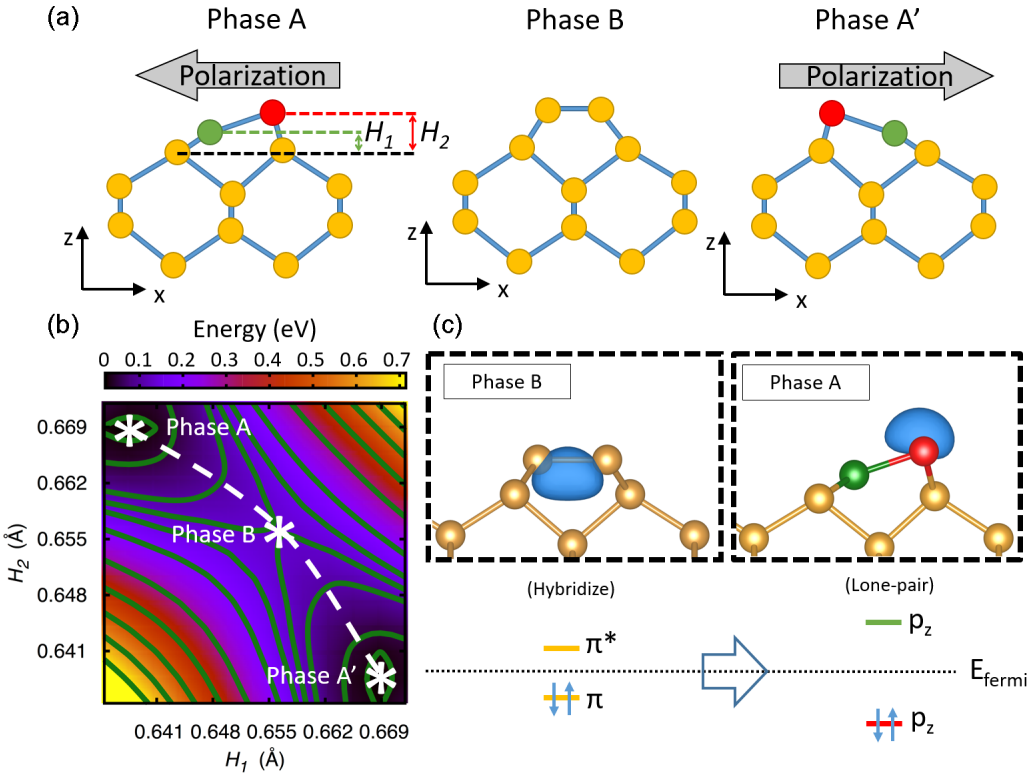

FIG. 1. (a) Side view of the reconstructed silicon (001) surface in $p(2 \times 1)$ configuration. The dimer atomic sites shifted up and down are colored as red and green, respectively. (b) Energy contour of the $p(2 \times 1)$ Si dimer, with respect to different site heights H_1 and H_2. (c) Upper panel: Wannier function plot for phase A and phase B with an isovalue of 8 a.u. Phase A demonstrates a lone pair formatting on the upper dimer atom and phase B shows a clear picture of p_z bonding orbitals (albeit conductive, this localized Wannier function plot was generated using the WANNIER90 package [17]). Lower panel: A sketch of bonding evolution.

and calculation showed consistently that the surface unit cell (u.c.) is made of two surface atoms in an asymmetric dimer configuration, which can buckle either to the left [Fig. 1(a) right] or to the right [Fig. 1(a) left]. The mechanism for the symmetry breaking is different from that for other 2D systems such as SnSe in which the two different sublattices naturally break the centrosymmetry. In contrast, here a Peierls instability leading to a gap opening, in line with the bulk properties of semiconducting silicon, is responsible for the buckling of the dimers and the emergence of electric dipoles [14–16].

We performed first-principles calculations based on the density functional theory (DFT). The calculation details are given in the Supplemental Material [17]. Our results confirm that the asymmetric dimer is indeed the most stable local structure for Si (001) at 0 K. (Detailed structure parameters can be found in Table S1 of the Supplemental Material [17].) For the sake of discussion, in Fig. 1(a) we denote the height of the left atom relative to its bulk position as H_1 and that of the right atom as H_2. If $H_1 < H_2$, the dimer buckles to the right (phase A). Otherwise, it buckles to the left (phase A′). The two phases are related to each other by a mirror operation, so they are equivalent. However, if A has a polarization of P, A′ must have an opposite polarization of $-P$. These properties fulfill the requirements of ferroelectricity. By varying H_1 and H_2 [Fig. 1(b)], we map out the energy landscape for Si (001), which exhibits a distinctive saddle point at $H_1 = H_2$ (denoted as phase B) with an energy barrier of 0.19 eV/u.c. in agreement with the previous work of 0.2 eV/u.c. [18]. We can use $dH = H_1 - H_2$ as an order parameter for the transition between A ($dH < 0$) and A′ ($dH > 0$). This simplifies the results in Fig. 1(b) to a characteristic anharmonic double-well potential-energy profile shown in Fig. 2(a) and Fig. S7(a) in the Supplemental Material [17], and also indicates a switchable twofold degenerate dipole state.

Note that phase B maintains the mirror symmetry of the dimer, while phases A and A′ do not. With the symmetry breaking, charge is transferred from the lower atom to the upper atom [as shown in Fig. 1(c) and Fig. S2 in the Supplemental Material [17]], accompanied by a dehybridization of the bonding p orbitals [Fig. 1(c)] [11,19]. This charge transfer lowers the system energy considerably and, as a result, creates a spontaneous electronic polarization. In other words, after the buckling, the upper atom is negatively charged while the lower atom is positively charged, leading to a nonzero electrical dipole moment P (Fig. S3 in the Supplemental Material [17]). The calculation of site polarization, however, is a bit tricky in this case. Because the reference centrosymmetric structure (phase B) is conductive, its dipole moment cannot be directly calculated using the Berry phase method. However, this does not correspond to the case when the so-called polarization quantum [20] diminishes due to the overlap of conduction and valence bands, and the polarization plot (dipole moment vs distortion) is still a multivalued function. Here, by calculating several distortions (from phase B towards phase A) using Berry phase method and linear fit of all nonmetal structures'

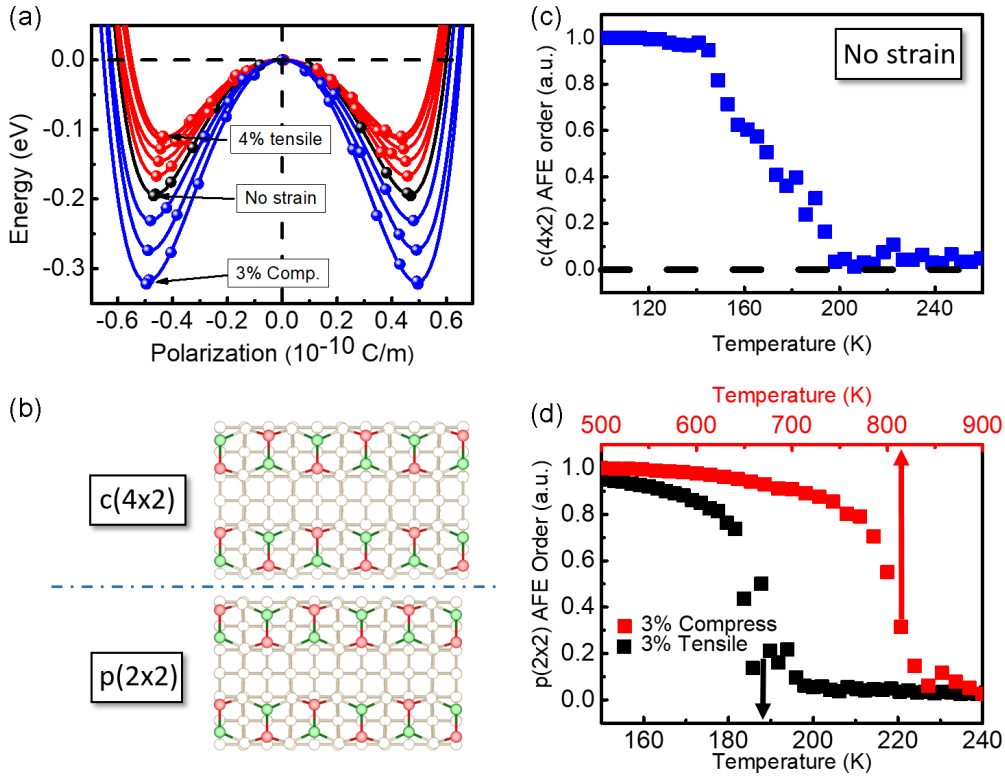

FIG. 2. (a) Double-well energy profile with respect to different strains; dots are DFT results and spline lines are Landau formula fits. (b) Top view of $c(4 \times 2)$ and $p(2 \times 2)$ dimer configurations. The dimer atomic sites shifted up and down are colored as red and green, respectively. (c), (d) Phase transition between $c(4 \times 2)$ AFE/$p(2 \times 2)$ AFE and PE phases in the Si (001) surface with and without strain. Relative order was calculated via Eq. (S4) in the Supplemental Material [17]. At low temperature, structure keeps its AFE order, while at high temperature thermal fluctuation breaks equilibrium and drives the system into the disordered PE phase.

dipole moment (Fig. 3), we extracted the dipole moment of the phase B structure and derived the polarization value for phase A/A′. We found the local structure possesses an in-plane local polarization of 0.45×10^{-10} C/m along the x axis (the out-of-plane polarization is small enough to be neglected). Interestingly, we also find that in phase B the valence and conduction bands have no degeneracy with one another at any point across the entire Brillouin zone. This means the valence band itself forms an isolated band set and it is possible to describe its charge centers using Wannier functions. Using the WANNIER90 package [21], we obtained the valence Wannier charge centers of phase B (Table S2 and Fig. S3 in the Supplemental Material [17]), confirming the value of the in-plane electrical polarization. The magnitude of this 2D polarization is robust and comparable to those in group-IV monochalcogenides monolayers [3] (which has been confirmed by experiment [7]) and other 2D ferroelectric materials [3–5].

Up until now, we only considered the geometric structure of one unit cell; this means we still do not know how dipole moments (or local structure) couple to each other. In ferro/antiferroelectricity, site coupling is very important. Without any couplings, on-site dipole moments cannot be orderly oriented without the help of external field; this means the system shall always stay in a paraelectric (PE) state. By calculating several configurations' total energy [Fig. 3(c) and Table I], we find the most stable intersite configuration (ground state) has a $c(4 \times 2)$ reconstruction [Fig. 2(b)] [22,23]. This finding means the most stable state can be achieved when the nearest-neighboring site has opposite buckle direction. Combined with our previous analysis of the on-site polarization, this $c(4 \times 2)$ configuration is antiferroelectric (AFE) [Figs. 2(b) and 3(c)]. In this picture, a uniformly oriented dipole moment (FE structure) corresponds to $p(2 \times 1)$ reconstruction [Fig. 3(c)] and its energy indicates that it is a metastable configuration comparing to the $c(4 \times 2)$ ground state (see Table I).

The temperature dependence of the ferroelectric phase is of importance, because it determines if the system can be used in practical applications. Experimentally, a random flipping of the dimer was observed for $T \geqslant 200$ K [12,23–25], and at around 900 K an emergence of metallic behavior due to a dynamic flip-flop of the canted dimers has been reported [26–28]. Although these observations constrain the ordered phases to low temperatures, below we will show that there are systematic ways to alter the phase's stability and achieve a ferroelectric performance at elevated temperatures.

To gain more insight into the structural relation between different dipole configurations, one needs to know the underlying energy relation between different configurations. Direct mapping of the energy profile for the system is a computational formidable task. Luckily, linking dH to the polarization, we only need a Hamiltonian connecting the system's total energy directly to the local polarization and the relative positions of neighboring sites. Previous study points out the effect of Si atoms underneath cannot be neglected for the

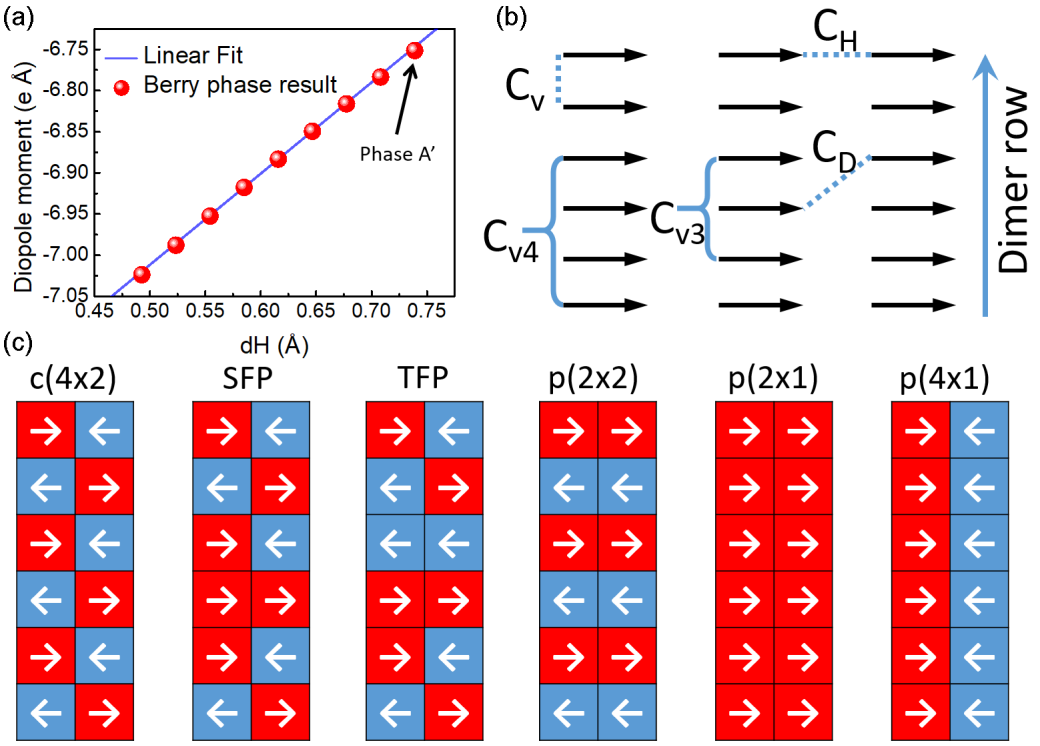

FIG. 3. (a) Linear fitting of dipole moment vs dH to estimate dipole moment in nonbuckled phase B ($dH = 0$). (b) A sketch of the coupling relation in the Si (001) reconstructed surface. The black arrow is the site polarization direction. (c) Schematic diagrams showing different configurations used in extracting model coefficients. The white arrow indicates the site polarization direction.

Si (001) surface and the second neighbor coupling as well as anisotropic coupling effect are also important [29]. Thus, a modified Landau model is built, which includes not only first but also second neighbor and the substrate local stress effect [Fig. 3(b)]. By calculating several configurations' total energies, these coefficients can be effectively extracted. Here, we construct a so-called discrete ϕ^4-like Hamiltonian [30], which takes the following form:

$$E = \sum_{i,j}\left[\frac{A}{2}\left(P_{i,j}^2\right) + \frac{B}{4}\left(P_{i,j}^4\right) + \frac{C}{6}\left(P_{i,j}^6\right) + \frac{D}{8}\left(P_{i,j}^8\right)\right] + \sum_{i,j} E_{\text{field}} P_{i,j} A_s + C_V \sum_{i,j} P_{i,j} P_{i,j+1} + C_H \sum_{i,j} P_{i,j} P_{i+1,j} + C_D \sum_{i,j} P_{i,j}\left(P_{i+1,j-1} + P_{i+1,j+1}\right) + \sum_i \langle C_{V3}\rangle_{3i} + \sum_i \langle C_{V4}\rangle_{4i}, \quad (1)$$

TABLE I. DFT calculated total energy of different surface configurations.

Parameters	No strain (eV)	3% compress (eV)	3% tensile (eV)
$c(4 \times 2)$	−1425.305547	−1416.150527	−1423.964987
$p(2 \times 1)$	−1424.238777	−1414.918007	−1423.53306
$p(2 \times 2)$	−1425.304907	−1416.381659	−1424.120787
$p(4 \times 1)$	−1423.859567	−1414.420721	−1423.307355
SFP	−1425.141118	−1415.9417	−1423.728572
TFP	−1425.155846	−1415.966306	−1423.974541

where P is the on-site polarization; i and j are the x-direction and y-direction labels of the unit cells, respectively; E_{field} is the external electric-field strength; A_s is the surface area; A, B, C, and D are the polynomial parameters; $\langle\rangle_{3i}$ and $\langle\rangle_{4i}$ denote the existence of three or four consecutive sites oriented at the same direction. The first four terms of the Hamiltonian are associated with the energy contributed by each unit cell and they well describe the on-site anharmonic double-well potential of our system [see Fig. 2(a) and Fig. S7(a) in the Supplemental Material [17]]. The last five terms are for the anisotropic nearest-neighbor interaction (C_v for vertical coupling and C_h for horizontal coupling), isotropic second nearest-neighbor interaction (C_D), and strain penalty terms (C_{v3} and C_{v4}) that can be modeled by an Ising-like model [12,29,31]. Specifically, C_{v3} and C_{v4} terms correspond to cases when multiple consecutive sites with same buckling (polarization) align across the y direction [dimer row direction in Fig. 3(b)]. They are necessary because the DFT energy calculation indicates large local stress energy. To accurately reflect this, energy terms C_{v3} (for three consecutive sites) and C_{v4} (for four consecutive sites) are added as penalty terms to the total energy [32]. We did not further include more consecutive site penalty terms, because the energy penalties for them are very high and they rarely exist. These last five terms are closely related to the order-disorder limit, and the 2D geometrical character is crucial for the ordering and the phase transition. The external electric-field effect on dipole is described within first-order approximation which will be discussed later. Expansion parameters are fitted by DFT calculations and all model parameters obtained from fitting are shown in Table II. To get the model coefficients from DFT

TABLE II. Coefficients for Eq. (1), fitted by DFT results.

	Si			Ge
Parameters	No strain	3% compress	3% tensile	No strain
Polarization $P_i(10^{-10}\,\mathrm{C/m})^2$	0.45	0.49	0.42	0.62
C_v (meV P_i^2)	37.37	65.31	10.59	17.91
C_h (meV P_i^2)	−15.77	−1.52	−7.95	−9.9
C_D (meV P_i^2)	−7.90	−2.77	−0.728	−5.1
C_{v3} (meV P_i^2)	14.83	−13.92	22.00	10.33
C_{v4} (meV P_i^2)	30.86	16.34	18.93	32.41
A [eV/(0.1 nC/m)^2]	−2.58	−4.96	−1.96	−2.81
B [eV/(0.1 nC/m)^2]	0.83	18.30	1.89	0.32
C [eV/(0.1 nC/m)^2]	2.32	1.55	3.79	17.53
D [eV/(0.1 nC/m)^2]	257.79	1.3	228.34	0.39

results, a set of configurations was used [Fig. 3(c)]. Based on the DFT calculated energy of these configurations, we estimate the coupling coefficients by

$$\begin{aligned} E_{c(4\times2)} &= -12C_V - 12C_H + 24C_D + \text{const} \\ E_{p(2\times2)} &= -12C_V + 12C_H - 24C_{D+} + \text{const} \\ E_{p(2\times1)} &= 12C_V + 12C_{V3} + 12C_{V4} + 12C_H + 24C_D + \text{const} \\ E_{p(4\times1)} &= 12C_V + 12C_{V3} + 12C_{V4} - 12C_H - 24C_D + \text{const} \\ E_{\mathrm{SDF}} &= -8C_V + C_{V3} - 8C_H + 16C_D + \text{const} \\ E_{\mathrm{TDF}} &= -8C_V - 4C_H + 8C_D + \text{const}. \end{aligned} \tag{2}$$

The coefficients A, B, C, and D are obtained by fitting the polynomial with the DFT calculated anharmonic double well. This effective Hamiltonian provides a starting point for studying the complicated configurations of the Si (001) surface from a thermodynamic perspective.

With the effective Hamiltonian carefully defined above, we are able to proceed to study temperature effect on the Si (001) surface. Detailed description of the MC method can be found in the Supplemental Material [17]. With 6000 MC steps (10 000 flip-flops in each MC step) at each temperature, the low-temperature $c(4\times2)$ AFE phase turns into the random PE phase at around 190 K [Fig. 2(c)], in good agreement with experimental observation [12,23–25].

Because of the low transition temperature T_c, silicon dimers suffer from severe flip-flop fluctuations at room temperature, resulting in random configurations across the surface. This makes it difficult for industrial application at room temperature. To solve this problem, we suggest a simple and feasible method to enhance the transition temperature by applying uniaxial strain to the substrate. It is noted that under both tensile and compressive strain the ground state of dimer configuration switched into $p(2\times2)$ "stripy" AFE configuration [see Fig. 2(b)]. Specifically, under 3% compressive strain, this $p(2\times2)$ stripy AFE configuration is more stable than $c(4\times2)$ AFE configuration with an energy difference of 20 meV/u.c. Meanwhile, the transition barrier height increases nearly twofold [Fig. 2(a)], from ∼0.19 to ∼0.34 eV under 3% compressive strain, and the polarization increases up to 0.5×10^{-10} C/m (Fig. S7 in the Supplemental Material [17]). As a result, the transition temperature calculated by MC is increased up to 800 K [Fig. 2(d)]. In contrast, tensile strain offers a possible way to decrease polarization and lowers the transition barrier. With tensile strain, this stripy AFE configuration is destroyed by thermal fluctuation at relatively low temperature [Fig. 2(d)], leaving a random configuration across the surface. Thus, the tensile strain can effectively weaken the dipole ordering by decreasing the coupling coefficient (Table II). Actually, the zero-polarization phase B [Fig. 1(a)] may even be achieved under large tensile strain [Fig. S7(b) in the Supplemental Material [17]]. Due to the thermal fluctuations and surface doping effect [12], the actual strain needed for this symmetric zero-polarization phase could be reduced. This strain correlated phase transition offers a possible explanation for the metallic behavior observed in experiment at high temperature (∼900 K) as the flat dimer of this symmetric phase causes the hybridization of p orbitals between two Si atoms of the dimer [28], making the surface conductive [Fig. 1(c)].

Ferro/antiferroelectricity requires that the polarization can be effectively tuned by external electric field. Combining our MC method with the approximation of first-order dipole–electrical-field interaction [Eq. (1) and Eq. (S5) in the Supplemental Material [17]], the relationship between dimer configurations and quasistatic alternating electric field can be obtained under different temperatures and strain conditions. As shown in Fig. 4, taking the strain-free Si (001) surface for example, at 100 K a FE type hysteresis loop occurs, contradicting the $c(4\times2)$ AFE ground state. This can be easily understood: the coupling energy dominates over the thermal fluctuation, resulting in an "energy barrier" to stabilize the metastable $p(2\times1)$ FE phase over the $c(4\times2)$ AFE phase (see Fig. S12 in the Supplemental Material [17]). In contrast, at 250 K, the thermal fluctuation is so strong that the coupling energy cannot sustain an ordered state. Interestingly, at 200 K, a double hysteresis loop occurs which corresponds to the appearance of the AFE phase. Taking a close look at 200 K, the system effectively enters an AFE phase which is constructed not only with the $c(4\times2)$ configuration but also with the $p(2\times2)$ configuration when the polarization becomes zero, as shown in the inset of the upper middle panel of Fig. 4. This is due to the metastable nature of $p(2\times2)$ dimer configuration: although the global minimum structure is $c(4\times2)$, $p(2\times2)$ configuration is only a few meV higher in energy than $c(4\times2)$ configuration, coinciding with a weak coupling in the x axis (C_h) compared to C_v (Table II). Both $c(4\times2)$ and $p(2\times2)$ configurations are AFE phases, which causes the appearance of a double hysteresis loop at 200 K.

The hysteresis loops can also be effectively manipulated by external strain. With 3% compressive strain applied at 200 K, the system under external electric field remains in a FE-like hysteresis loop (lower panel of Fig. 4). The coercive field, which is the external electric field needed to completely reverse the total polarization, is around 0.05 V/Å. In contrast, the strain-free system at 200 K already enters the AFE state (indicated by the appearance of a double hysteresis loop) which does not have a coercive field. Under 3% compressive strain, the shape of the double hysteresis loop can be clearly distinguished at room temperature (300 K), indicating an enhanced coupling and a higher pseudo energy barrier (large

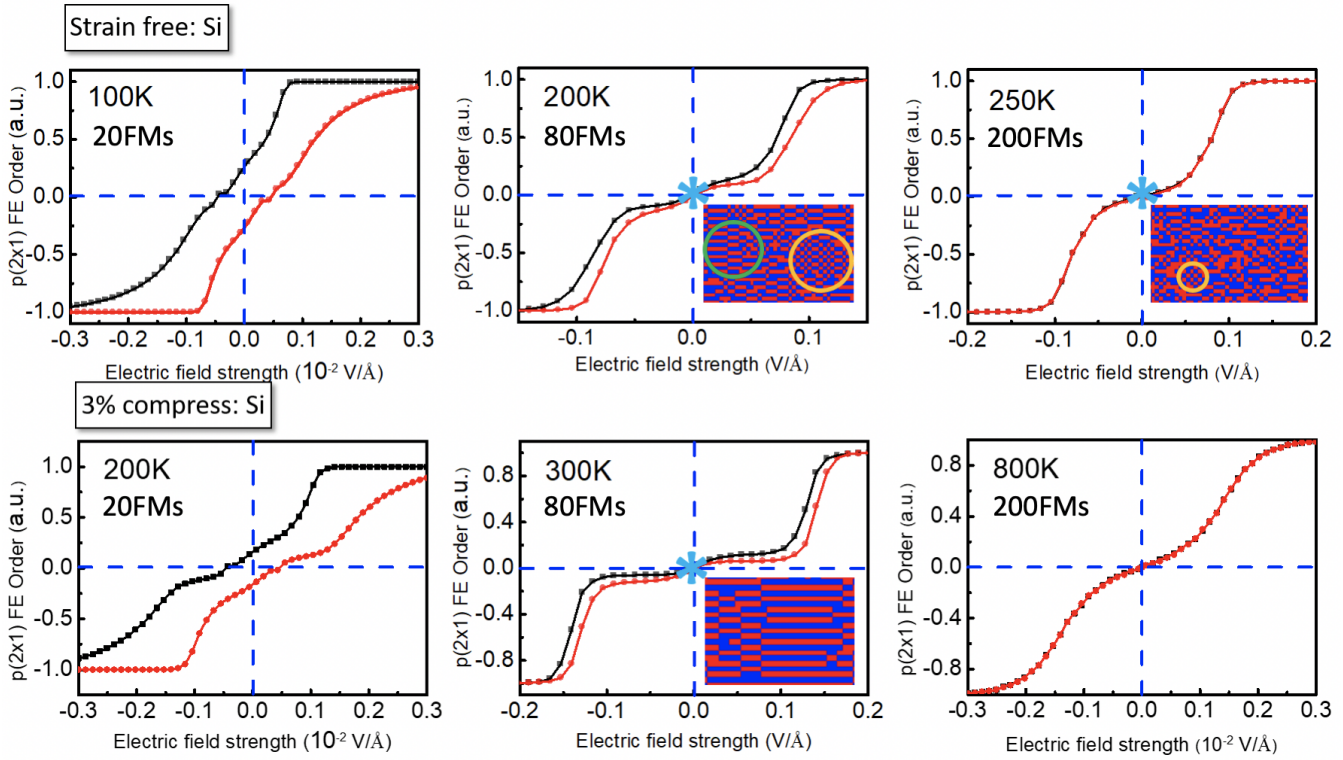

FIG. 4. Dielectric response of silicon surface dimers under different temperatures, calculated via Monte Carlo method; FMs is the number of flip-flop motion performed during the hysteresis simulation; and the electrical polarization is represented as relative order described in Eq. (S4) in the Supplemental Material [17]. Insets: Configurations corresponding to the * mark, where the yellow and green circle contain $c(4 \times 2)$ and $p(2 \times 2)$ dimer configurations separately.

C_v in Table II) inside this strained surface dimer system. It is noted that the ground state of the Si (001) surface dimer becomes a $p(2 \times 2)$ stripy AFE phase under compressive strain, resulting in more stripy AFE contribution than others of the zero-field structure in the double hysteresis loop (inset in lower middle panel of Fig. 4). On the other hand, with a 3% tensile strain applied, the system effectively enters the PE state below 200 K due to the weakened coupling between sites. Thus, the coupling between dipoles of each site is extremely sensitive to the local and substrate strain, which can also be discerned from the dramatic changes in C_3 and C_4 coupling coefficients under strain (Table II). The saturation field (minimum external electric field to saturate ferroelectric polarization) is also sensitive to the strain and temperature and, at same temperature, the compressive strain causes a moderate enhancement of this saturation field while tensile stain reduces it (Fig. S8 in the Supplemental Material [17]). As a result, the ferroelectric hysteresis loops can be controlled easily by strain.

It is possible to utilize this ferroelectric surface as a way to manipulate current. One example is illustrated in Fig. 5(a). In this "shoulder to shoulder" domain configuration, the domain polarization vectors are either parallel or antiparallel between neighboring domains. With different domain configurations, the transport properties can be easily switched. Considering a two-domain/two-terminal device, the transmission spectra differ for different domain configurations as shown in the lower panel of Fig. 5(a). With a voltage of 1 V applied, the antiparallel domain configuration shows a current of 2.12 nA, around twice higher than the current of 0.96 nA for the parallel configuration. This indicates two switchable resistive states and suggests that more gates can induce more switchable resistive states. By calculating the transmission spectra of four-gate and multigate configuration, we confirm it is indeed the case (Fig. S5 in the Supplemental Material [17]).

On the other hand, the electric polarization can also generate charge accumulation at the FE domain boundaries. In Fig. 5(b), we construct a supercell along the polarization direction and the polarization has been reversed for a few adjacent unit cells to form a domain boundary. In this way, two different channel regions ("head-to-head" and "tail-to-tail") appear [left panel of Fig. 5(b)]. The calculated unit-cell-resolved total density of states (DOS) are shown in the right panel of Fig. 5(b). The boundary region exhibits metallic characteristics instead of their intrinsic insulating nature. Specifically, electrons accumulate at the "head-to-head" boundary while holes gather at the other, indicating that the FE polarization derived charge transfer is hindered at the domain boundary and forms interfacial conductive states. This result confirms yet again the existence of in-plane FE in the silicon (001) surface, and suggests a potential way to differentiate the orientations of different FE domains in experiment.

In conclusion, using first-principles calculation, we predict that the reconstructed silicon (001) surface is electrically polarized with an in-plane 2D polarization of 0.45×10^{-10} C/m. Calculated Curie temperature is around 190 K and can be drastically tuned via external strain. The dielectric response

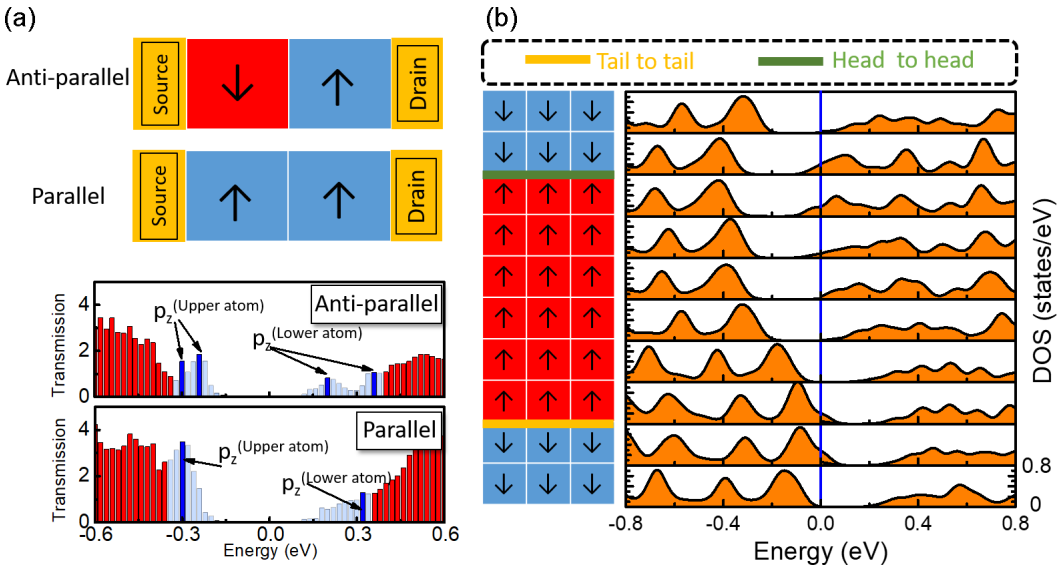

FIG. 5. (a) Upper panel: Schematic view of a two-gate device as described in the main text. Lower panel: Transmission spectrum calculated with different gate configurations. It is clear that the p_z band splitting in antiparallel configuration made CBM and VBM closer to Fermi energy. (b) Ferroelectric boundary perpendicular to the dimer row direction; the left panel shows a sketch of one "head to head" type boundary and one "tail to tail" type boundary, while the right panel shows the projected density of states for different dimer rows.

for the system shows an AFE-like double hysteresis loop, which may be further utilized for potential-energy storage devices. The carrier type and transport properties of boundaries between domains can be readily manipulated by electric gate or field, resulting in different transport behavior and on/off ratio. Our paper provides an example of surface ferroelectricity for an elemental material system, and it reveals a surprising hidden property for one of the most well-known surface systems. In view of the dominating role played by Si in the semiconducting industry, the findings here can have a huge impact in developing electronic functional devices.

This work was supported by the National Natural Science Foundation of China (Grant No. 61574123), the Fundamental Research Funds for the Central Universities, and Zhejiang Provincial Natural Science Foundation (Grant No. D19A040001).

[1] N. Nuraje and K. Su, Nanoscale **5**, 8752 (2013).
[2] O. Auciello, J. F. Scott, and R. Ramesh, Phys. Today **51**, 22 (1998).
[3] R. Fei, W. Kang, and L. Yang, Phys. Rev. Lett. **117**, 097601 (2016).
[4] K. Chang, J. Liu, H. Lin, N. Wang, K. Zhao, A. Zhang, F. Jin, Y. Zhong, X. Hu, W. Duan, Q. Zhang, L. Fu, Q. Xue, X. Chen, and S. Ji, Science **353**, 274 (2016).
[5] M. Wu and X. C. Zeng, Nano Lett. **16**, 3236 (2016).
[6] P. Z. Hanakata, A. Carvalho, D. K. Campbell, and H. S. Park, Phys. Rev. B **94**, 035304 (2016).
[7] C. Xiao, F. Wang, S. A. Yang, Y. Lu, Y. Feng, and S. Zhang, Adv. Funct. Mater. **28**, 1707383 (2018).
[8] B. J. Kooi and B. Noheda, Science **353**, 221 (2016).
[9] K. Shportko, S. Kremers, M. Woda, D. Lencer, J. Robertson, and M. Wuttig, Nat. Mater. **7**, 653 (2008).
[10] Y. Wang, C. Xiao, M. Chen, C. Hua, J. Zhou, C. Wu, J. Jiang, S. A. Yang, Y. Lu, and W. Ji, Mater. Horiz. **5**, 521 (2018).
[11] P. Kruger and J. Pollmann, Phys. Rev. Lett. **74**, 1155 (1995).
[12] K. Inoue, Y. Morikawa, K. Terakura, and M. Nakayama, Phys. Rev. B **49**, 14774 (1994).
[13] K. Hata, Y. Sainoo, and H. Shigekawa, Phys. Rev. Lett. **86**, 3084 (2001).
[14] K. Seino, W. G. Schmidt, and F. Bechstedt, Phys. Rev. Lett. **93**, 036101 (2004).
[15] X. Ren, H. Kim, C. Niu, Y Jia, and J. Cho, Sci. Rep. **6**, 27868 (2016).
[16] W. G. Schmidt and K. Seino, Curr. Appl. Phys. **6**, 331 (2006).
[17] See Supplemental Material at http://link.aps.org/supplemental/10.1103/PhysRevMaterials.3.044410 for detailed description of Wannier interpolation, transmission calculation, model fit, and Monte-Carlo method as well as other calculated data.
[18] A. Ramstad, G. Brocks, and P. J. Kelly, Phys. Rev. B **51**, 14504 (1995).
[19] G. K. Wertheim, D. M. Riffe, J. E. Rowe, and P. H. Citrin, Phys. Rev. Lett. **67**, 120 (1991).
[20] N. A. Spaldin, J. Solid State Chem. **195**, 2 (2012).
[21] N. Marzari and D. Vanderbilt, Phys. Rev. B **56**, 12847 (1997).
[22] Y. J. Li, H. Nomura, N. Ozaki, Y. Naitoh, M. Kageshima, Y. Sugawara, C. Hobbs, and L. Kantorovich, Phys. Rev. Lett. **96**, 106104 (2006).
[23] M. Kubota and Y. Murata, Phys. Rev. B **49**, 4810 (1994).
[24] K. C. Low and C. K. Ong, Phys. Rev. B **50**, 5352 (1994).
[25] T. Tabata, T. Aruga, and Y. Murata, Surf. Sci. **179**, L63 (1987).
[26] J. H. Cho and J. Y. Lee, Phys. Rev. B **71**, 075307 (2005).

[27] Y. Fukaya and Y. Shigeta, Phys. Rev. Lett. **91**, 126103 (2003).
[28] M. Rohlfing, P. Kruger, and J. Pollmann, Phys. Rev. B **52**, 13753 (1995).
[29] D. Pillay, B. Stewart, C. B. Shin, and G. S. Hwang, Surf. Sci. **554**, 150 (2004).
[30] A. D. Bruce, Adv. Phys. **29**, 111 (1980).
[31] J. Ihm, D. H. Lee, J. D. Joannopoulos, and J. J. Xiong, Phys. Rev. Lett. **51**, 1872 (1983).
[32] H. Kawai, Y. Yoshimoto, H. Shima, Y. Nakamura, and M. Tsukada, J. Phys. Soc. Jpn. **71**, 2192 (2002).